Experimental and numerical investigation of HyperVapotron heat transfer

2014 Nucl. Fusion 54 123004

(http://iopscience.iop.org/0029-5515/54/12/123004)

IOP Publishing | International Atomic Energy Agency Nuclear Fusion
Nucl. Fusion **54** (2014) 123004 (10pp) doi:10.1088/0029-5515/54/12/123004

Experimental and numerical investigation of HyperVapotron heat transfer

Weihua Wang[1,2], Haifei Deng[1,2], Shenghong Huang[3], Delin Chu[1], Bin Yang[1], Luoqin Mei[1] and Baoguo Pan[1]

[1] New Star Institute of Applied Technology, Hefei, Anhui 230031, People's Republic of China
[2] Institute of Plasma Physics, Chinese Academy of Sciences, Hefei, Anhui 230031, People's Republic of China
[3] University of Science and Technology of China, Hefei, Anhui 230026, People's Republic of China

E-mail: whwang@ipp.cas.cn

Received 28 February 2014, revised 7 August 2014
Accepted for publication 19 August 2014
Published 16 October 2014

Abstract

The divertor first wall and neutral beam injection (NBI) components of tokamak devices require high heat flux removal up to 20–30 MW m^{-2} for future fusion reactors. The water cooled HyperVapotron (HV) structure, which relies on internal grooves or fins and boiling heat transfer to maximize the heat transfer capability, is the most promising candidate. The HV devices, that are able to transfer large amounts of heat (1–20 MW m^{-2}) efficiently, have therefore been developed specifically for this application. Until recently, there have been few attempts to observe the detailed bubble characteristics and vortex evolvement of coolant flowing inside their various parts and understand of the internal two-phase complex heat transfer mechanism behind the vapotron effect. This research builds the experimental facilities of HyperVapotron Loop-I (HVL-I) and Pressure Water HyperVapotron Loop-II (PWHL-II) to implement the subcooled boiling principle experiment in terms of typical flow parameters, geometrical parameters of test section and surface heat flux, which are similar to those of the ITER-like first wall and NBI components (EAST and MAST). The multiphase flow and heat transfer phenomena on the surface of grooves and triangular fins when the subcooled water flowed through were observed and measured with the planar laser induced fluorescence (PLIF) and high-speed photography (HSP) techniques. Particle image velocimetry (PIV) was selected to reveal vortex formation, the flow structure that promotes the vapotron effect during subcooled boiling. The coolant flow data for contributing to the understanding of the vapotron phenomenon and the assessment of how the design and operational conditions that might affect the thermal performance of the devices were collected and analysed. The subcooled flow boiling model and methods of HV heat transfer adopted in the considered computational fluid dynamics (CFD) code were evaluated by comparing the calculated wall temperatures with the experimentally measured values. It was discovered that the bubble and vortex characteristics in the HV are clearly heavily dependent on the internal geometry, flow conditions and input heat flux. The evaporation latent heat is the primary heat transfer mechanism of HV flow under the condition of high heat flux, and the heat transfer through convection is very limited. The percentage of wall heat flux going into vapour production is almost 70%. These relationships between the flow phenomena and thermal performance of the HV device are essential to study the mechanisms for the flow structure alterations for design optimization and improvements of the ITER-like devices' water cooling structure and plasma facing components for future fusion reactors.

Keywords: HyperVapotron devices, subcooled boiling experiment, heat transfer, numerical simulation

(Some figures may appear in colour only in the online journal)

1. Introduction

High heat flux components of fusion reactors, such as divertor first wall and neutral beam injection (NBI) components of tokamak devices, require heat flux removal up to 20–30 MW m^{-2} [1–4]. The water cooled HyperVapotron (HV) structure, which relies on internal grooves or fins and boiling heat transfer to maximize the heat transfer capability, is the most promising candidate. HV devices, that are able to transfer large amounts of heat (1–20 MW m^{-2}) efficiently, have therefore been developed specifically for this application. In HV devices, the flow field and temperature field are greatly influenced by the bubble behaviour such as the formation, development, departure and coalescence, and also influenced by vortex behaviour inside their various parts. The phase change and interfacial tension between liquid phase and vapour phase will cause exchanges of mass, energy and momentum, which makes heat transfer extremely complicated [5–7].

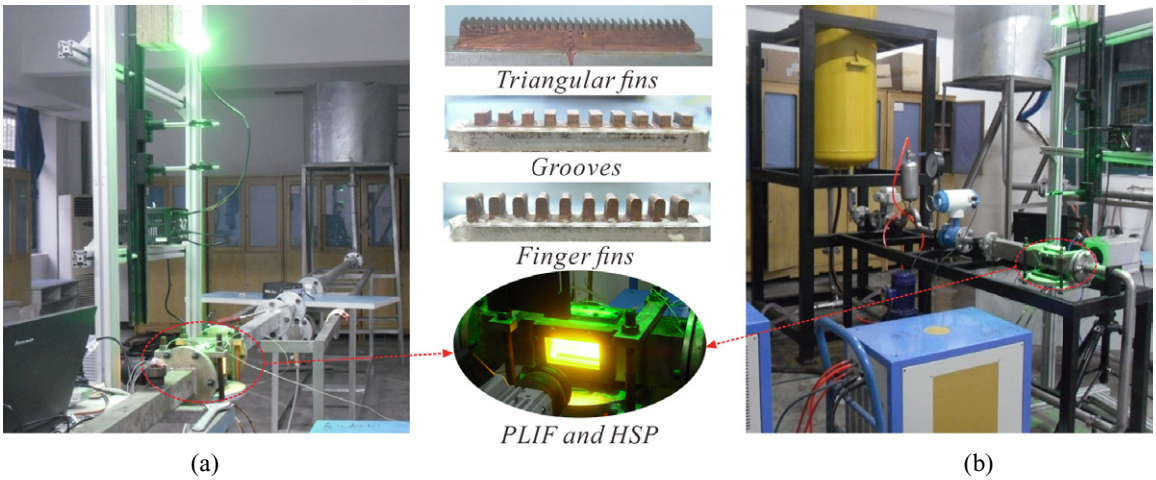

Figure 1. Experimental facilities of HVL-I (*a*) and PWHL-II (*b*).

Until recently, there have been few attempts to observe the detailed vortex form and bubble behaviour of coolant flowing inside their various parts and understand the internal two-phase complex heat transfer mechanism behind the vapotron effect. The experimental research on related issues is mostly simple instead of observing microscopic flow field and vortex formation [8, 9]. As for the numerical simulation of phase change, which is the extension of the experiment, current literature focuses mainly on the study of bubble characteristics in pool boiling under conditions of ordinary pressure and low heat flux, and study of HV heat transfer under high heat flux and high pressure conditions is lacking [10–12].

The cooling channel heat sink structure of the ITER first wall and NBI (EAST and MAST) are designed as squares or rectangles and directly welded with CuCrZr and stainless steel. The HV heat transfer structure is applied in the internal CuCrZr wall on which the regular grooves, fins and roughened surface block the water flow and cause partial boundary refluxes. The vast majority of heat flux is taken away by the HV latent heat, so the structural temperature of the wall is no higher than the permitted operating temperature.

This research implements the experiment and numerical simulation of HV enhanced heat transfer, aiming at the components facing the plasma high heat flux in the fusion reactor, especially those with 'enhanced' thermal load such as the ITER divertor and NBI. Although the ultimate goal is to develop HV technology of ITER-like device water cooling structure, according to the principle of HV heat transfer, we start with experiment and analyse in some detail the simple cases of triangular fins and grooves in a rectangular channel. Therefore, the HyperVapotron Loop-I (HVL-I) has been set up to implement the subcooled boiling principle experiment in term of typical flow parameters and geometrical parameters of the test section, which is heated on one side. Considering the pressure water operating conditions (0.7–3 MPa) of ITER-like devices, the closed Pressure Water Hypervapotron Loop-II (PWHL-II) has been constructed to implement the high heat flux HV heat transfer correlative experiment for divertor first wall and NBI components (geometries reflect the MAST and the EAST HV sections at full scale). The multiphase flow and heat transfer phenomena on the surface of triangular fins and grooves, when the subcooled water flowed through, have been observed and measured with planar laser induced fluorescence (PLIF) and high-speed photography techniques (HSP). Particle image velocimetry (PIV) was selected to reveal vortex formation, the flow structure that promotes the vapotron effect during subcooled boiling. The experimental study has been carried out to collect coolant flow field, temperature field data and flow images for contributing to the understanding of the vapour phenomenon and the assessment of how the design and operational conditions that might affect the thermal performance of the devices. The numerical simulation model and methods of HV heat transfer adopted in the considered CFD code are evaluated by comparing the calculated wall temperatures with the experimental values. The results and methodology will provide technical support for design optimization and improvements of ITER-like device water cooling structure and plasma facing components for future fusion reactors.

2. Experiment

2.1. Experimental facilities

According to the development requirements of HV sections of reactor components such as the first wall, NBI component and other heat exchanger engineering devices, the experimental facilities of high heat flux HV heat transfer were established in China. These include HVL-I, with the work pressure of 0.1 MPa, and PWHL-II, in which the work pressure of fluid is up to 3 MPa. As shown in figure 1, they consist of subsystems of flow control, heating and data acquisition. The flow control subsystem includes a pressure water pump, electromagnetism digital flow meter, test section and stainless steel pipelines. The heating subsystem includes the high-frequency electromagnetism induction heating source of input heat flux (1–10 MW m^{-2}) and the temperature control module. The data acquisition subsystem includes the temperature acquisition module, the PIV module, the PLIF module and the HSP.

Table 1. Test cases and experimental conditions.

Cases	Experimental facility	HV geometry	Working pressure (bar)	Inflow water velocity ($m\,s^{-1}$)	Input heat flux ($MW\,m^{-2}$)	Measurement technologies
Case 1	HVL-I	Triangular fin	1	0.3	1.06	HSP
Case 2	HVL-I	Triangular fin	1	0.3	1.86	HSP
Case 3	HVL-I	Groove	1	1.1	3.57	PLIF + HSP
Case 4	HVL-I	Groove	1	1.1	4.82	PLIF + HSP
Case 5	HVL-I	Triangular fin	1	0.6	—	HSP + PIV
Case 6	PWHL-II	Groove	7	1–3	1.48–2.27	HSP

2.2. Measurement technologies

As shown in figure 1, in the PLIF light path, the input beam is from a 2 W 532 nm continuous wave laser, which works as a light source. The light spot is dispersed by a lenticular lens into a 1 mm light sheet and enters the test section through the optical glass above. The working fluid is the rhodamine B aqueous solution, which emits fluorescence when induced by a light sheet laser. A 580 ± 20 nm narrow band pass filter is installed before the lens of the high-speed camera to filter out all other light except the fluorescence acquired in HSP. A PIV method is selected to reveal instantaneous vortex formation, the flow patterns that promote the vapotron effect during subcooled boiling, which relies on using PLIF to form an almost one dimensional light sheet inside the flow region of interest (figure 1). The flow is uniformly 'seeded' with 1 μm sized SiO_2 particles. A microscopic camera with HSP is used to record the positions of the seeding particle when illuminated by the laser light sheet. In the temperature acquisition subsystem, a 0.5 mm diameter K-type thermocouple is installed on the base of the fin or groove to measure the temperature there and to provide feedback signals for heating for temperature control. An eight-channel ART DAM-3039 card is applied in the temperature acquisition module to monitor in real time the temperature changes in all channels through a compiling program. The relationship between the temperature of the rhodamine B aqueous solution and the intensity of the fluorescence is calibrated in the test section to obtain the temperature of the working fluid. The temperature is fitted linearly with fluorescence intensities in the measured temperature range; the linear correlation coefficient R is about 0.9946. The fitted linear equation is given as $G = -1.4222\,T + 101.21$, where T is the temperature and G is the grey level.

2.3. Experimental cases

As shown in table 1, six typical test cases were selected for experiments using different experimental facilities and measurement technologies under different conditions. From case 1 to case 5, the HVL-I was used. In case 1 and case 2, subcooled boiling multiphase flows in triangular fins under different heat fluxes were observed by HSP. In case 3 and case 4, subcooled boiling multiphase flows in grooves under different heat fluxes were measured by the HSP with PLIF as well. In case 5, PLIF and PIV measurement methods were added. In case 6, PWHL-II was selected, the coolant pressure was increased up to 0.7 MPa and the temperature distributions in grooves were measured under different heat fluxes and different flow velocities (such as ITER first wall, EAST and MAST NBI HV structures). Because the heat resistance of the thermal insulation component connecting the fins and grooves and the test section are limited, the current maximum input heat flux is less than $5\,MW\,m^{-2}$, and it will be increased to $20\,MW\,m^{-2}$ in the next step.

2.4. Experimental results and discussion

2.4.1. Flow patterns of triangular fins under different heat fluxes. In figure 2, a large number of vapour bubbles were generated near the fin surfaces when the subcooled water flowed through. Generally, there are two types of vapour bubble. The first type has a relatively large diameter, residing temporally on the base and top of triangular fin and then moving into water with relatively low frequencies. These bubbles moved into fluid in parabolic trajectories, with a relatively quick upward velocity due to buoyancy. It was also observed along the trajectories that the shape of the moving bubble became slender and the volume was reduced gradually, which might be attributed to the effects of buoyancy and drag forces as well as the condensing of vapour in bubbles. The second type has a relatively small diameter, moving quickly into water with relatively high frequencies and moving downstream with adjacent fluid. The number of these small bubbles was very large, so a pattern like fog was formed (bubble-fog) when they were wrapped and clustered by a fluid vortex, indicating a violent subcooled boiling. These experimental phenomena are in accordance with the simulation results (see figure 15(*a*)). Comparing the different heat fluxes of case 1 and case 2, with the change of the heat flux, the number and flow pattern of vapour bubbles were different. With the increase of input heat flux, more vapour bubbles with smaller size were generated, which was indicated as more intense bubble-fog patterns in the image, and simultaneously the departure frequencies of bubbles were obviously increased, leading to an increase of number density as well as the diffusing region of the bubbles.

2.4.2. PLIF measurement flow patterns of grooves. Figure 3 is the instantaneous greyscale PLIF image recorded by HSP, in which the subcooled water flowing through has been observed and measured in case 3 and case 4. The geometry of the grooves is designed similarly to the NBI component of the EAST and MAST. Many dark spots moving like clouds occurred in the adjacent region of grooves. This was a result of the reduction of the fluorescence intensity due to heat transferring from the groove to the water and increase of the local temperature in the water. According to the relationship between temperature and grey level (see section 2.2), it is reasonable to find that the region with the highest temperature is located near the groove

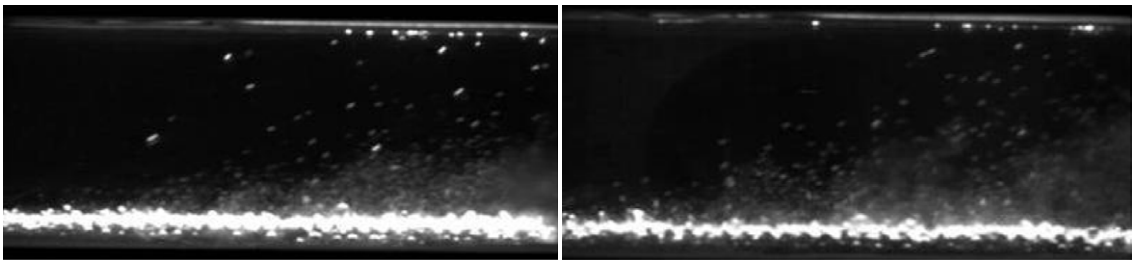

(a) (b)

Figure 2. Flow images of triangular fins under different heat fluxes of case 1 (*a*) and case 2 (*b*).

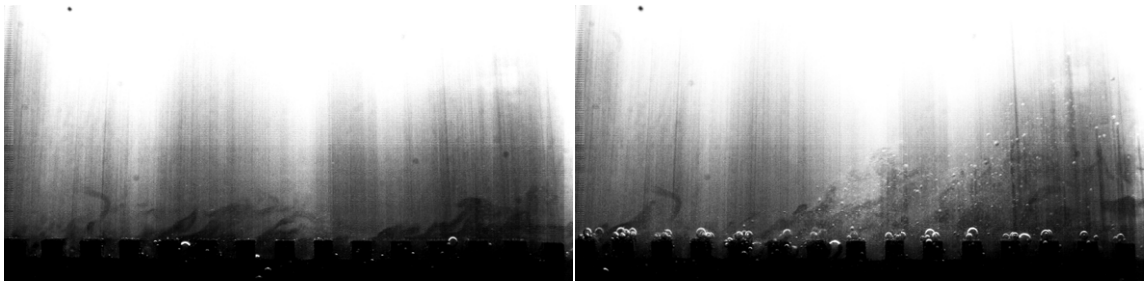

(a) (b)

Figure 3. Instantaneous greyscale PLIF images of HV grooves in case 3 (heat flux 3.3 MW m^{-2}, (*a*)) and case 4 (heat flux 4.56 MW m^{-2}, (*b*)).

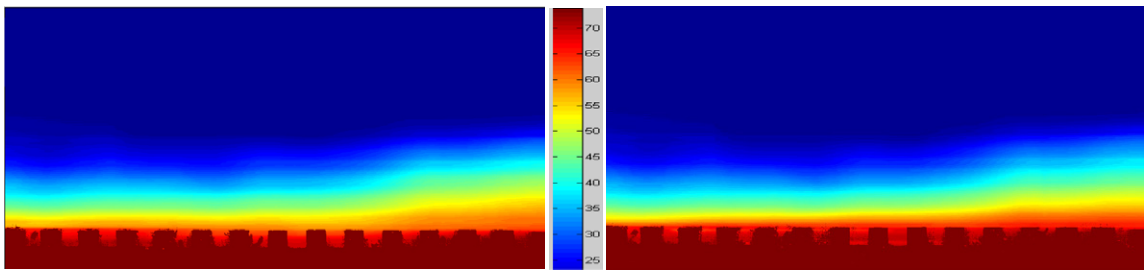

(a) (b)

Figure 4. Averaged temperature field in case 3 (heat flux 3.3 MW m^{-2}, (*a*)) and case 4 (heat flux 4.56 MW m^{-2}, (*b*)).

surfaces (darkest region). In contrast, in the region of no heat transfer and constant temperature (region far from grooves), no dark spots occur and the grey levels remain unchanged. The moving patterns of dark spots or clouds also indicate the movement of locally heated flow adjacent to grooves surface. The density is locally decreased and upward acceleration is obtained due to buoyancy. This movement is coupled with a local vortex generated by the grooves, presenting a series of coherent structure patterns near the groove surface and indicating a typical feature of heat transfer enhancement by a local vortex of grooves.

Figure 4 is the colour image of the averaged temperature field, which was obtained by averaging all instantaneous temperature contours processed from PLIF pictures of 2 s (recorded at 500 fps by HSP), through calculating the calibrated linear relationship by applying the calibration procedure according to methods provided by [13]. It shows that the temperature near the grooves ranges mostly from 60 to 80 °C, which is less than the corresponding saturated temperature of 100 °C, indicating a typical subcooled boiling. The heat flux of the measured plane was obtained by applying a gradient computation to the mean temperature contour (figure 4); only about 0.3–1.2 MW m^{-2} heat flux was transferred to the water fluid adjacent to the groove surface through heat convection, far less than the input heat flux of 3.3–4.6 MW m^{-2} at the groove base. The primary input heat flux should be transferred through evaporation of subcooled boiling. Comparing the magnitude of convective heat flux with input heat flux, it is clear that the heat transfer through phase change accounts for most of the total heat input in the HV process. The percentage of wall heat flux going into vapour production is about 65–72%.

2.4.3. PIV measurement of the flow vortex form. HV thermal performance may be due to the vortex behaviour, such as vortex form, centroid location, breakup events and stability. Microscopic cameras with HSP and PIV methods were used to study the effects of the vortex interaction with the free-stream (see figure 1). These methods provide vortex measurement with high spatial resolution, which identified the flow structure

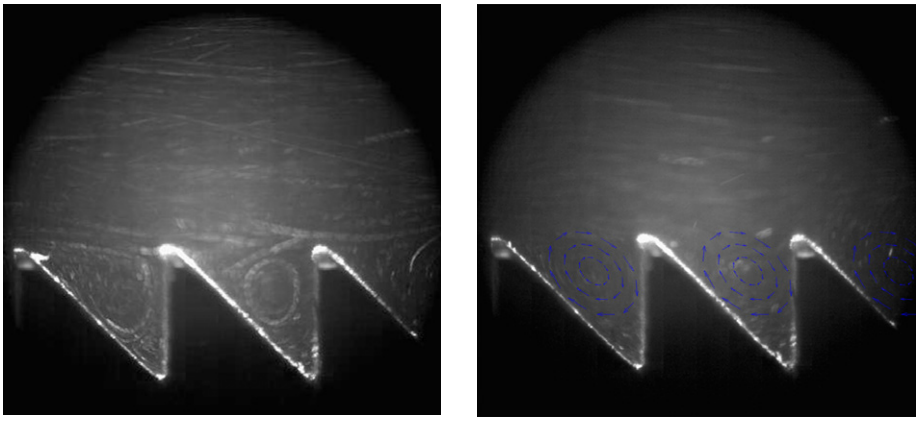

Figure 5. Instantaneous vortex interaction with the free-stream image recorded by PIV and HSP with microscopic cameras in case 5.

that may promote the vapotron effect. As shown in figure 5, the magnitude of the vortex interaction with the free-stream flow, the flow pattern, and the vortex form, centroid location, breakup events and stability were observed in case 5. It is discovered that, with the increase of the free-stream flow velocity, the vortex rotary speed and breakup events increase, the centroid location of the vortex accelerates upward to half of the fins, and the vortex becomes more unstable, which might be attributed to the effects of the radial momentum of the free-stream and spin momentum of the vortex. One transverse vortex exists per HV groove, and interacts dynamically with the free-stream. When the input heat flux increases, the bubble density is locally increased and the upward acceleration is obtained due to buoyancy. This movement is coupled with a local vortex generated by fins indicating a typical feature of heat transfer enhancement by a local vortex (figure 5). Comparing the triangle fin and groove, the vortex becomes more circular in grooves. The shallower grooves exhibit a less circular, more slowly rotating, less stable vortex. Further, it is proposed that the flow structure altering property of HV devices can be exploited to establish better understanding and enhance the thermal performance of the HV devices.

2.4.4. Pressurized water subcooled boiling patterns of grooves. In order to demonstrate ITER-like first wall and NBI HV enhanced heat transfer, PWHL-II was established, and the coolant pressure was increased up to 0.7 MPa; the temperature distributions in the grooves were measured under different heat fluxes and different flow velocities in case 6. In the next step of the experiment, the coolant pressure and input heat flux are increased to 2 MPa and 20 MW m^{-2} respectively. Figure 6 presents the approximate linearity relationship between the heat flux and the control temperature measured on the test section base, which is used to control the high-frequency electromagnetism induction heating source of input heat flux, under the different flow velocities. The experimental results demonstrate that when the coolant flow velocity increases by 1 m s^{-1} the heat flux will increase by 5–8%, which indicates the cooling capability enhanced by HV in the flow process. Comparing with the ordinary pressure water HV devices, with the working pressure increase the saturation temperature increases (the saturation temperature of water is 165 °C at 0.7 MPa) and the critical heat flux will increase, but an enhanced heat transfer capability is unapparent.

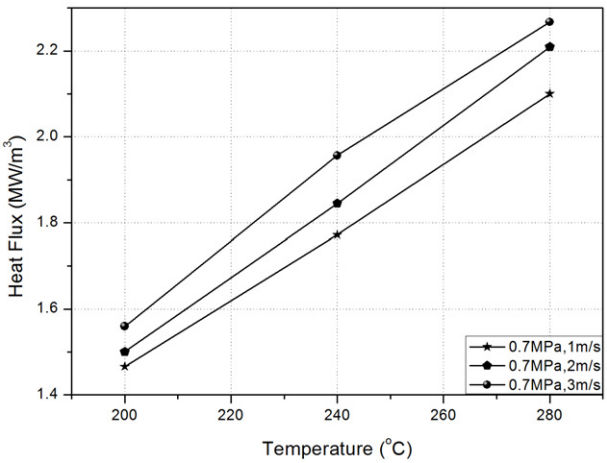

Figure 6. The relationship between the heat flux and the control temperature at the different flow velocities in case 6.

3. Numerical simulation

There are several papers have been devoted during the last few years to the simulation of HV heat transfer in different geometries foreseen for the ITER-like devices [14–18]. Even though substantial information can be extracted regarding the thermal performance under a given thermal loading for different geometries, the computational work has not been evaluated due to the lack of high resolution experimental data to compliment the bubble and vortex properties of the investigations performed and hence provide further insight into the physics of the vapotron effect. To account for the two-phase (liquid–vapour) nature of the HV flow, we have the inhomogeneous Eulerian method and the volume of fluid (VOF) method. The Eulerian method assumes that the liquid and vapour phases are interpenetrating continua, resolving each phase separately. The Eulerian method combined with the Rohsenow model can solve the HV two-phase flow nucleate boiling heat transfer accurately. Gravity and surface tension are included, but a relatively large number of cells with a higher computational cost and using a boiling model to extrapolate near wall values are its problems [19].

The VOF method for film boiling is based on an enhancement of the Rohsenow model [20] and on the

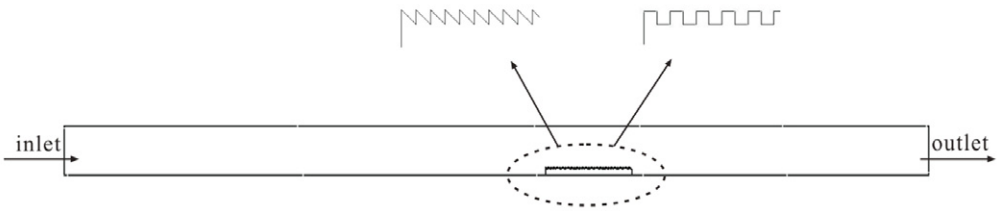

Figure 7. Geometric model of the flow channel and the triangular fins or grooves.

classical Bergles–Rohsenow (BR) work [21]. Because the BR model solving for one phase only is computationally less expensive than the Rohsenow one, we select it as the current computation model to help better assessment of the experimental phenomenon, so that predictive models can be developed to guide the engineering design of the HV devices.

3.1. Modelling

According to the analysis of the flow characteristics of the working fluid, turbulent flow occurs near the triangular fins and grooves. Turbulent flow was accounted for by the realizable k–ε model, with wall-functions to handle $y^+ \sim 30$ near the wall. It is appropriate to apply the k–ε model for the transient calculation of the flow and heat transfer process by comparing the calculation accuracy between different turbulence models, such as shear stress transport (SST) k–ω Reynolds Averaged Navier Stokes (RANS) turbulence models.

3.1.1. VOF method and FLUENT BR model. The VOF method is applied for the formation and disappearance process of the bubbles in HV heat transfer. It is a surface-tracking technique applied to a fixed mesh. We implemented the BR model in the FLUENT code, specifically by using a user-defined function (UDF) program, and then compared computed results with our experimental data. FLUENT considers a single fluid (liquid), with an ad hoc prescription for the heat transfer coefficient (HTC) in the subcooled boiling region, following the BR treatment. A single set of momentum equations is shared by the fluids, and the volume fraction of each of the fluids in each computational cell is tracked throughout the domain. Surface tension is not present in the model, due to the limited density variation with temperature in the liquid phase. A more recent and accurate correlation for bubble departure frequency is selected by Situ *et al* [22].

3.1.2. Source term of control equation.

(1) Mass source term. According to the Lee model [23], when the saturation temperature is taken as the boundary, the direction and amount of mass transfer is as shown in equation (1). If the control volume temperature T is higher than the saturation temperature T_{sat}, the liquid phase mass in the control volume decreases and the corresponding vapour phase mass increases. The mass transfers from liquid phase to vapour phase for evaporation of the liquid phase. If $T < T_{\mathrm{sat}}$, the vapour phase mass in the control volume decreases and the corresponding liquid phase mass increases. The mass transfers from vapour phase to liquid phase for condensation of vapour phase. This is shown here:

$$S_{\mathrm{m}} = \begin{cases} \frac{r_{\mathrm{l}}\alpha_{\mathrm{l}}\rho_{\mathrm{l}}(T-T_{\mathrm{sat}})}{T_{\mathrm{sat}}} & T \geqslant T_{\mathrm{sat}} \\ \frac{r_{\mathrm{v}}\alpha_{\mathrm{v}}\rho_{\mathrm{v}}(T-T_{\mathrm{sat}})}{T_{\mathrm{sat}}} & T < T_{\mathrm{sat}} \end{cases} \quad (1)$$

where r_{l} and r_{v} are the mutual conversion coefficients of the liquid phase and vapour phase respectively. α_{l} and α_{v} are the volume fractions of the liquid phase and vapour phase respectively. ρ_{l} and ρ_{v} are the densities of the liquid phase and vapour phase respectively.

(2) Energy source term. The energy source term is obtained by the mass source term of evaporation and condensation multiplying the corresponding latent heat of evaporation under the working pressure.

$$S = h_{\mathrm{fg}} S_{\mathrm{m}} \quad (2)$$

where h_{fg} is the latent heat from the liquid phase to the vapour phase.

With the help of FLUENT software in the commercial CFD platform, UDFs can be developed according to equations (1) and (2). The source terms above are added to the control equation of the BR model through the UDF interface to calculate the liquid phase mass source term, vapour phase mass source term and phase transformation energy source term in all cells.

3.2. Geometric model and boundary conditions

3.2.1. Geometric model and mesh. The geometric model is shown in figure 7; the size of the flow channel is 900 mm × 50 mm and that of the base of the triangular fin or groove is 90 mm × 5 mm; these have 30 sets of triangular fins or 15 sets of grooves with the size of 3 mm × 3 mm respectively. The boundary conditions of the velocity inlet and free outflow outlet and the heating surface of constant temperature are applied. After piecewise meshing the flow channel and establishing a boundary layer on the fin or groove surface, the density of the mesh on the surface is locally increased, as is shown in figure 8.

To calculate the heat flux of the fins or grooves accurately, the structural meshes are divided to the greatest extent on the fins or grooves created with the commercial mesh generator GAMBIT. A mesh accuracy test demonstrates, when the mesh total number adds from 0.5 to 1.5 mega cells, that the calculation accuracy error is reduced to ∼5%. Considering a good compromise between reasonable grid-independence of the solution and computational cost, the mesh size of the fluid boundary layer is increased gradually from 0.03 to 0.3 mm between the wall and free-stream. This size of the mesh is also comparable to that chosen in previously published works on

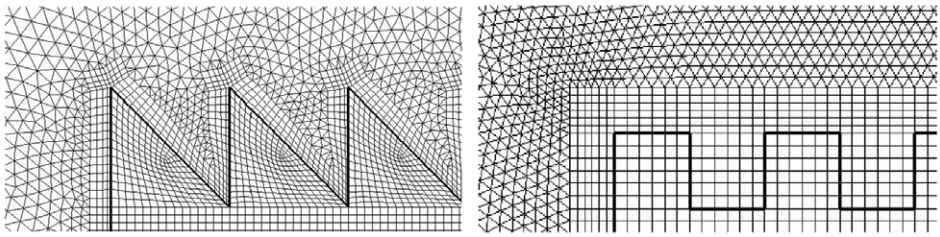

Figure 8. Boundary layer and local mesh of triangular fins and grooves.

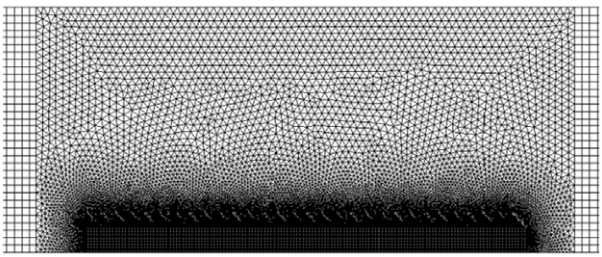

Figure 9. Local flow channel mesh on the fins.

the same subject [14, 19]. Then the local flow channel mesh on the fins is shown in figure 9, and the mesh accuracy meets the requirement by the mesh sensitivity test.

To estimate the heat flux of the triangular fins and grooves, eight vertical monitor points with 1 mm separation and four vertical monitor points with 2 mm separation are selected respectively in the model and their temperatures are recorded, as is shown in figure 10.

3.2.2. Boundary conditions and calculation parameters. Suppose the liquid phase and vapour phase are both incompressible Newtonian fluids; the physical property of water is determined by the inlet temperature and working pressure. The physical property of vapour is the saturated vapour property corresponding to the working pressure. Heat flux is applied through adiabatic boundaries (walls) surrounding the domain. Take case 2 and case 3 in the experiment as the verification model, in which the material of the flow channel surface is steel as the adiabatic wall, the material of the triangular fins and grooves is CuCrZr, and the inlet velocity and outlet boundary conditions are selected as in table 1.

3.3. Calculation results and discussion

3.3.1. Calculation results. Figure 11 is the contours of velocity magnitude near triangular fins and grooves. The velocity above the triangular fins and grooves obviously increases because the flow channel becomes narrow. Figures 11(a) and (b) show the velocity distribution of the test section in case 2 and case 3, and the average velocities of the free-stream are about 0.3 m s^{-1} and 1.1 m s^{-1} respectively. The calculation results accord with experimental values. Figure 12 shows the velocity vector and vortex form inside their various parts of the triangular fins and grooves. The velocities of the flow field are reduced by a steady eddy in the middle region of the triangular fins and grooves. In general, one transverse vortex exists per triangular fin or groove to interact dynamically with the free-stream. The vortexes detach from the free-stream flow and move between the triangular fins and grooves, and the centroid location of the vortex accelerates half way up the fins and grooves. The fluid exchange from free-stream to vortex is much more pronounced in different geometries. The vortex form of figure 12(a) is similar to the instantaneous vortex form image recorded by PIV and HSP with microscopic cameras in case 5 (figure 5).

Figure 13 is the static temperature contours near the triangular fins and grooves. The saturation temperature of water under the current conditions is 373 K. The temperature of water obviously rises near the fin and groove surfaces, while the temperature in the rest of the flow field does not change significantly, which shows it is in a typical HV state. Figure 14 is the contour diagram of temperature in a region near the fins and grooves. The fins and grooves are 3 mm high. The base of the fins and grooves has been wrapped by bubbles. The temperatures of the triangular fin and groove surfaces are obviously higher than the saturation temperature, but the temperatures of the region about 1 mm above the triangular fins and grooves are less than the saturation temperature. The calculation results are beneficial to explain the experimental phenomenon in detail (figure 4).

Figure 15 shows the volume fraction of bubbles near the triangular fins and grooves. The boundary conditions of the calculation are similar to those of case 2 (b) and case 3 (a). Comparing with the experimental observations of figures 2(b) and 3(a), it is indicated that a certain number of large bubbles are attached to both the base and the top of the triangular fins and grooves, and gradually at a lower rate fall into the cooling water. Among them, some bubbles coalesce and become slender and larger and move upwards along a parabolic trajectory. Between the various parts of the triangular fins and grooves, there are numerous bubbles with a relatively small diameter, moving quickly into the water with relatively high frequencies and moving downstream with adjacent fluid. The bubble formation and evolution phenomena of the simulation are similar to experimental observation. Comparatively, the density of the bubble-fog of case 3 is higher than that of case 2, which indicates that the latent heat of evaporation of case 3 is higher.

3.3.2. Heat flux. The relationship between heat flux and heat conductivity coefficient is $Q = \sigma\ \Delta T/d$, where σ is the material heat conductivity coefficient, and ΔT and d are the temperature difference and the distance between two measured points respectively. Heat fluxes are calculated using the temperature difference between measured points

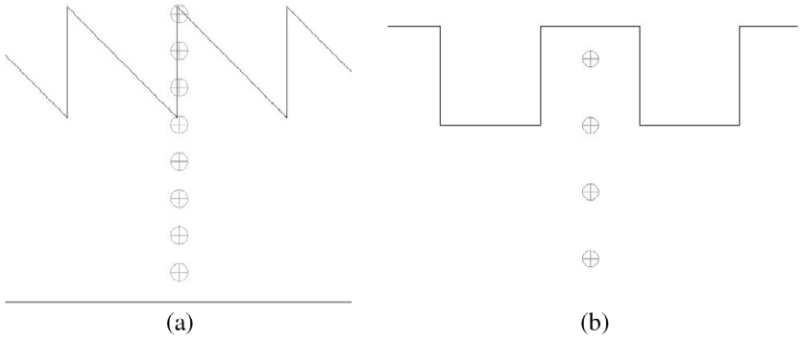

Figure 10. Temperature monitor scenario of triangular fins (*a*) and grooves (*b*).

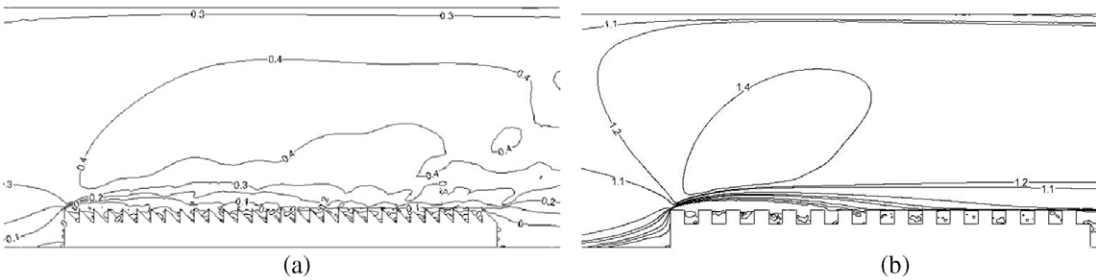

Figure 11. Velocity magnitude of the triangular fins and grooves in case 2 (*a*) and case 3 (*b*).

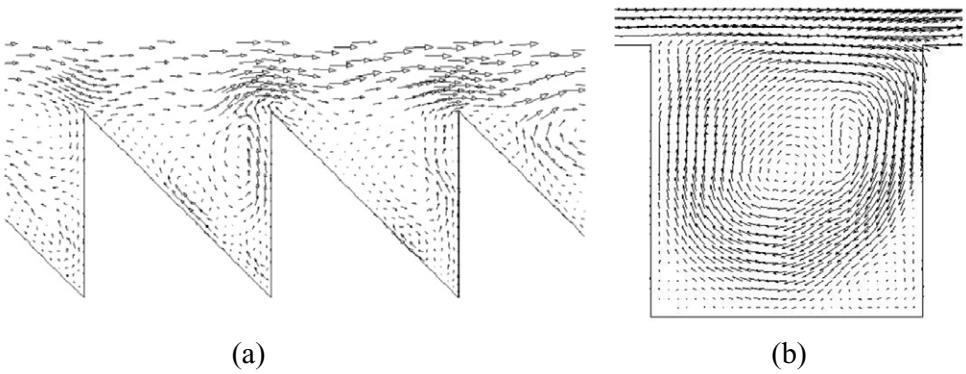

Figure 12. Velocity vector and vortex form near the triangular fins and grooves in case 2 (*a*) and case 3 (*b*).

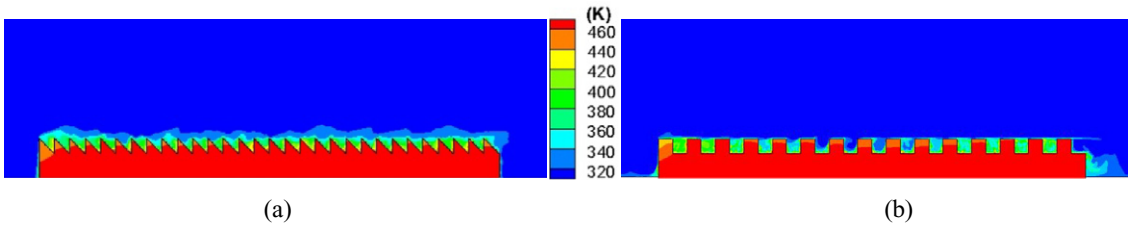

Figure 13. Static temperature contour of the triangular fins and grooves in case 2 (*a*) and case 3 (*b*).

and monitored points (figure 10). The heat flux values of calculation and experimentally measurement are presented in figure 16; the transverse coordinate is the monitor point temperature of the test section base, which is used to control the high-frequency electromagnetism induction heating source of input heat flux. The experimentally measured values of input heat flux are slightly higher than the calculation values, and the error range is between 11.2 and 19.7%. This is because in the experiment only four measured points selected to monitor the temperature are near to each other, which possibly causes measurement error. In addition, the heat source is discontinuous in the experimental process, so the base temperature of the grooves or triangular fins cannot maintain invariance. Considering this difference from the experiment, the calculation results can be taken as a reference for the experimentally measured values. Comparing the

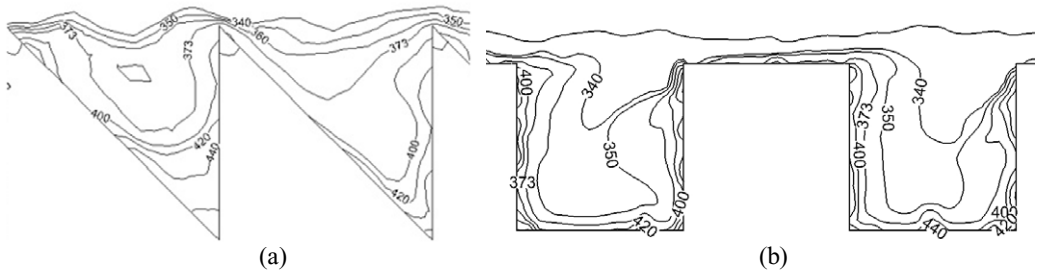

Figure 14. Contour diagram of temperature in a region near the triangular fins and grooves (K) in case 2 (*a*) and case 3 (*b*).

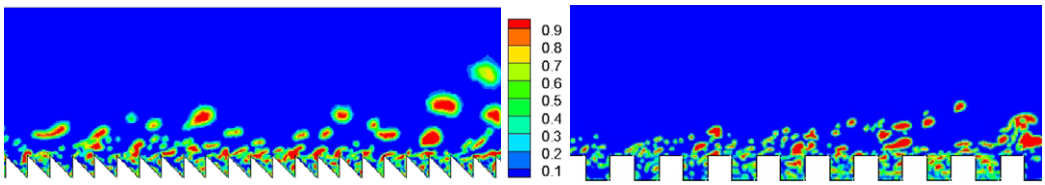

Figure 15. Volume fraction of bubbles of the triangular fins and grooves (%)in case 2 (*a*) and case 3 (*b*).

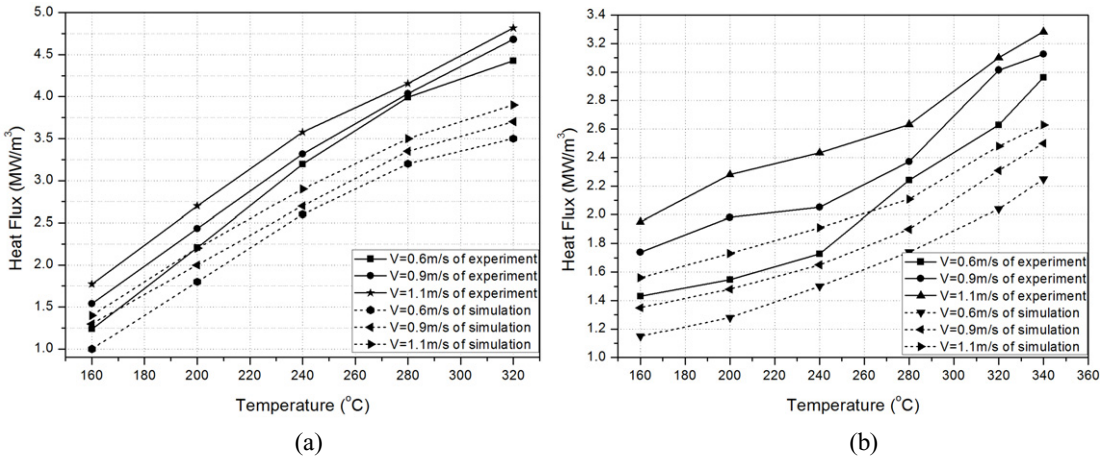

Figure 16. Comparing the heat flux of calculation results and measured values for grooves (*a*) and triangular fins (*b*).

experimentally measured values and the calculation results (figures 16(*a*) and (*b*)), when the input heat fluxes are same, the temperature of the test section base of the grooves is less than that of the triangular fins. It is indicated that the enhanced heat transfer ability of the grooves is higher than that of the triangular fins under conditions of similar HV geometry and flow parameters, and the rate is about 20–70%.

4. Conclusions

In the present work, experimental facilities of high heat flux HV heat transfer have been established and the subcooled boiling principle experiment was implemented in terms of typical flow parameters, geometrical parameters of the test section and surface heat flux. PLIF with HSP and PIV with HSP are very helpful measurement techniques to investigate the multiphase flow of HV quantitatively. Through these measurement techniques, complicated and interesting phenomena of multiphase flow in HV process were observed, and the temperature distribution, the vortex formation and bubble behaviours in the flow field were measured quantitatively in a non-intrusive manner, validating the feasibility of applying non-intrusive measurement techniques in HV investigations and providing a powerful way to understand the multiphase heat transfer mechanism of HV in depth.

It has been demonstrated that the bubble and vortex characteristics in the HV are clearly heavily dependent on the internal geometry, flow conditions and input heat flux. The evaporation latent heat is the primary heat transfer mechanism of HV flow under the condition of high heat flux, and the heat transfer through convection is very limited. The percentage of wall heat flux going into vapour production is almost 70%. The high frequency of bubble departure and smaller bubble sizes are beneficial towards the overall thermal performance of the HV device. The enhanced heat transfer ability of the grooves is higher than triangular fins under the conditions of similar HV geometry and flow parameters, and the rate is about 20–70%. The experimental techniques obtained in this study can be used to measure the proportional distribution of heat flux through evaporation and convection quantitatively.

The numerical model and method of HV subcooled boiling enhanced heat transfer based on the commercial CFD platform were established. The interface of liquid and vapour was captured by the VOF method, and the phase change process was accomplished through the UDF to describe the mass and energy transportation. Comparing the experiment and numerical simulation results, the principle of subcooled boiling heat transfer and the law of enhanced heat transfer are analysed. It is concluded that the BR model with transitions to VOF for film boiling should be preferred, provided a suitable experimental database is available to tune its relatively large number of free parameters. The BR model can also capture in that case, as for the flat channel, the main features of the fluid flow and heat transfer phenomena. Predictive models can be developed to guide the engineering design of the HV devices.

The present work is devoted to prototype experimental facilities and advanced measurement technique development for HV components in China. The next step of the research will focus on the following: (a) synchronous measurements of temperature field, vortex behaviour and bubble movement through PLIF and PIV techniques, which will be helpful in element design and optimization of HV components; (b) assessment of the potential for water-based nanofluids to improve HV performance; (c) increase of the pressure of the fluid similar to ITER-like component work conditions, to further understand the relationship between the principal HV flow structure and its heat transfer performance, by experimental studies in conjunction with CFD analysis.

Acknowledgments

This work is supported by the National Magnetic Confinement Fusion Science Program of China under grants Nos 2013GB113004 and 2013GB113000 and also by the National Natural Science Foundation of China with grants No 91326101.

References

[1] ITER Design Description Document, WBS 1.7, DIVERTOR, 13 July 2001
[2] Sergis A., Hardalupas Y. and Barrett T.R. 2013 Potential for improvement in high heat flux HyperVapotron element performance using nanofluids *Nucl. Fusion* **53** 113019
[3] Bobin-Vastra I. *et al* 2005 Activity of the European high heat flux test facility: FE200 *Fusion Eng. Des.* **75–79** 357–63
[4] Escourbiac F. *et al* 2005 A mature industrial solution for ITER divertor plasma facing components: hypervapotron cooling concept adapted to Tore Supra flat tile technology *Fusion Eng. Des.* **75–79** 387–90
[5] Yun B.J. 2010 Characteristics of the local bubble parameters of a subcooled boiling flow in an annulus *Nucl. Eng. Des.* **240** 2295–303
[6] Lee W.H. 1980 A pressure iteration scheme for two-phase flow modeling *Multiphase Transport Fundamentals, Reactor Safety, Applications* vol 1, ed T.N. Veziroglu (Washington, DC: Hemisphere)
[7] Huang S.H. *et al* 2013 Experimental study of hypervapotron under conditions of high heat flux *Sci. China Technol. Sci.* **56** 222–7
[8] Peipei Chen Ty., Newell A. and Barclay Jones G. 2008 Heat transfer characteristics in subcooled flow boiling with hypervapotron *Ann. Nucl. Energy* **35** 1159–66
[9] Yang Z., Peng X.F. and Ye P. 2008 Numerical and experimental investigation of two phase flow during boiling in a coiled tube *Int. J. Heat Mass Transfer* **51** 1003–16
[10] Son G. and Dhir V.K. 2008 Numerical simulation of nucleate boiling on a horizontal surface at high heat fluxes *Int. J. Heat Mass Transfer* **51** 2566–82
[11] Yang Z.L. *et al* 2000 Numerical investigation of bubble coalescence characteristics under nucleate boiling condition by a lattice-boltzmann model *Int. J. Therm. Sci.* **39** 1–17
[12] Heo S., Koshizuka S. and Oka Y. 2002 Numerical analysis of boiling on high heat-flux and high subcooling condition using MPS-MAFL *Int. J. Heat Mass Transfer* **45** 2633–42
[13] Du R.P. *et al* 2007 Measurement of temperature field in a fast liquid−liquid mixing process by PLIF *Chin. J. Process Eng.* **7** 859–64 (in Chinese)
[14] Wei J.H. *et al* 2012 VOF simulation of bubble characteristics of subcooled flow boiling *Nucl. Power Eng.* **33** 61–4
[15] Youchison D.L., Ulrickson M.A. and Bullock J.H. 2011 Prediction of critical heat flux in water-cooled plasma facing components using computational fluid dynamics *Fusion Sci. Technol.* **60** 177–84 (www.ans.org/pubs/journals/fst/a_12348)
[16] Ying A. *et al* 2010 3D CFD analysis of subcooled flow boiling heat transfer with hypervapotron configurations for ITER first wall designs *Fusion Eng. Des.* **85** 1348–53
[17] Domalapally P. *et al* 2012 CFD analysis of flow boiling in the ITER first wall *Fusion Eng. Des.* **87** 556–60
[18] Tao L. *et al* 2010 Numerical analysis of a cooling system for high heat flux components in the neutral beam injection system *Fusion Eng. Des.* **85** 2095–9
[19] Milnes J., Burns A. and Drikakis D. 2012 Computational modelling of the HyperVapotron cooling technique *Fusion Eng. Des.* **87** 1647–61
[20] Rohsenow W.M. 1952 A method of correlation heat transfer data for surface boiling of liquid *Trans. ASME* **74** 969–76
[21] Bergles A.E. and Rohsenow W.M. 1964 The determination of forced convection surface boiling heat transfer *J. Heat Transfer* **86** 365–72
[22] Situ R., Ishii M., Hibiki T., Tu J.Y., Yeoh G.H. and Mori M. 2008 Bubble departure frequency in forced convective subcooled boiling flow *Int. J. Heat Mass Transfer* **51** 6268–82
[23] Lee T.H. *et al* 2009 Axial developments of interfacial area and void concentration profiles in subcooled boiling flow of water *Int. J. Heat Mass Transfer* **52** 473–87